Phase Change Convective Heat Transfer in High Porosity Cellular Metal Foams

Y. Tian [a], C.Y. Zhao [b], Q. Wang [b]

[a] School of Engineering, University of Warwick, CV4 7AL Coventry, United Kingdom
Email: Y.Tian.4@warwick.ac.uk, Tel: +44 2476 522654

[b] School of Mechanical Engineering, Shanghai Jiaotong University, 200240 Shanghai, China

ABSTRACT

This Chapter discusses phase change convective heat transfer of high porosity cellular metal foams and their practical applications in thermal energy storage (TES). The following theoretical aspects are covered: volume-averaging method, Brinkman-Forchheimer porous flow model, two-equation non-thermal equilibrium heat transfer model, enthalpy method, and phase field method. Based on these models, metal foams have been investigated in two applications: metal foam-embedded phase change materials (PCMs), and metal foam-enhanced cascaded TES. The results indicate that metal foams can improve heat and exergy transfer rates in these applications by factors between 2 and 10.

Keywords: Metal Foam; Heat Transfer Enhancement; Volume-averaging Method; Permeability; PCM; Phase Field Model.

Cited as:

Y. Tian, C.Y. Zhao, Q. Wang. Phase Change Convective Heat Transfer in High Porosity Cellular Metal Foams. In Book: *Focus on Porous Media Research*. Nova Science Publishers Inc., New York, 2013 (ISBN: 978-1-62618-668-2).

1. INTRODUCTION

Thermal Energy Storage (TES) plays a pivotal role in utilising intermittent energy sources, especially solar energy. TES relies on Phase Change Materials (PCMs) of high heat storage capacities. However, most PCMs suffer from the common problem of low thermal conductivities, being around 0.2 W/(mK) for most paraffin waxes and 0.5 W/(mK) for most inorganic salts (Zalba et al., 2003).

High porosity metal foams (Zhao et al., 2010; Zhou and Zhao, 2011) have been proposed to enhance heat transfer in PCMs. This Chapter will investigate the transport phenomena in metal foam-embedded PCMs, involving phase change, coupled conductive and convective heat transfer, and metal foam modelling.

2. FLUID MECHANICS

2.1. Volume-averaging Method

Transport phenomena, such as fluid flow and heat transfer, are rather difficult to be quantified in porous media because of their complicated porous structures (shown in Figure 1). The volume-averaging method is usually employed by researchers when modelling transport phenomena in porous media. Volume-averaging method treats porous media as a continuous structure comprising many Representative Elementary Volumes (REVs). The size of an REV should be much larger than the characteristic pore size, so that a function *f* can have a reliable average value over a whole REV (Whitaker, 1969): volume-averaged value will fluctuate when REV is not large enough. The size of an REV should also be much smaller than the porous media macroscopic size, so that the differential equations that are used to describe transport phenomena in porous media can be applied to an REV (Whitaker, 1969). The volume-averaged value of function *f* is given by:

$$\langle f \rangle_{REV} = \frac{1}{V_{REV}} \int_{REV} f \, dV \tag{1}$$

Here, $\langle \ \rangle$ denotes the volume-averaged value of a certain function over an REV.

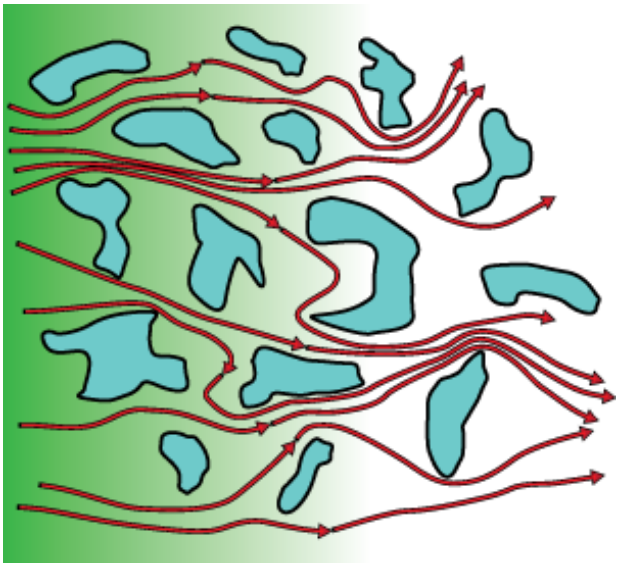

Figure 1. Flow in porous media (Laboratory for Scientific Computing, 2010).

2.2. Equations of Fluid Dynamics

2.2.1. Continuity Equation

The introduction of REV makes the traditional Fluid Dynamics equations applicable to metal foams. The Continuity Equation is given by:

$$\nabla \bullet \langle \mathbf{V} \rangle = \mathbf{0} \tag{2}$$

Eq. (2) takes on different forms under different coordinate systems, and its form under the Cartesian coordinate system can be written by:

$$\frac{\partial u}{\partial x} + \frac{\partial v}{\partial y} = 0 \tag{3}$$

Here, u and v denote the components of the velocity $\mathbf{V}$ in the x and y direction respectively.

2.2.2. Momentum Equation

Darcy's Law has been used to describe fluid flow through porous media for over a hundred years; however, its application has been restricted to seepage flow where flow velocity is rather low. Fluid flow in metal foams is usually at a much higher flow rate due to high porosities (85% and higher), resulting in the non-Darcy effects of viscous flow resistance and inertia flow resistance. To consider these non-Darcy effects, correction

terms have been introduced, and these include Brinkman correction for viscous effects (Brinkman, 1947) and Forchheimer correction for inertia effects (Forchheimer, 1901). Brinkman-Forchheimer extended Darcy Equations for metal foams take on the following form:

$$\frac{1}{\varepsilon}\langle\rho_f\rangle\frac{\partial\mathbf{V}}{\partial t}+\frac{\langle\rho_f\rangle}{\varepsilon^2}\langle(\mathbf{V}\bullet\nabla)\mathbf{V}\rangle= -\nabla\langle P\rangle+\frac{\mu_f}{\varepsilon}\nabla^2\langle\mathbf{V}\rangle-\frac{\mu_f}{K}\langle\mathbf{V}\rangle-\frac{\rho_f C_f}{\sqrt{K}}\|\langle\mathbf{V}\rangle\|\langle\mathbf{V}\rangle+\langle\rho_f\rangle\mathbf{g} \tag{4}$$

Here, $\|\ \|$ denotes the norm of a vector, $\mathbf{g}$ denotes the gravity vector, ε denotes the porosity of the metal foam, μ_f denotes the dynamic viscosity of the PCM, ρ_f denotes the density of the PCM, K is the permeability coefficient for homogeneous metal foams, which can be a vector/tensor for anisotropic materials, and C_f denotes the inertial factor for fluid flow in metal foams.

Eq. (4) takes on the following forms under the Cartesian coordinate system:

$$\rho_f\frac{\partial u}{\partial t}+\frac{\rho_f}{\varepsilon}\left(u\frac{\partial u}{\partial x}+v\frac{\partial u}{\partial y}\right)= -\frac{\partial p}{\partial x}+\frac{\mu_f}{\varepsilon}\left(\frac{\partial^2 u}{\partial x^2}+\frac{\partial^2 u}{\partial y^2}\right)-\frac{\mu_f}{K}u-\frac{\rho_f C_f}{\sqrt{K}}|u|u \tag{5}$$

$$\rho_f\frac{\partial v}{\partial t}+\frac{\rho_f}{\varepsilon}\left(u\frac{\partial v}{\partial x}+v\frac{\partial v}{\partial y}\right)= -\frac{\partial p}{\partial y}+\frac{\mu_f}{\varepsilon}\left(\frac{\partial^2 v}{\partial x^2}+\frac{\partial^2 v}{\partial y^2}\right)-\frac{\mu_f}{K}v-\frac{\rho_f C_f}{\sqrt{K}}|v|v+\rho_f g\varepsilon\beta(T_f-T_{ref}) \tag{6}$$

Here, $|\ |$ denotes the modulus of a variable. β denotes the thermal expansion coefficient of the PCM and T_f denotes the temperature of the PCM. The last term on the right hand side of Eq. (6) represents the buoyancy force caused by temperature differences of the PCM, and it is the driving force of the natural convection. The intensity of the natural convection in the PCM mainly depends on two factors: its driving force and resisting force (Tian and Zhao, 2011a). The driving force increases with increasing temperature differences, whilst the resisting force can be reduced by decreasing the viscosity μ_f of the PCM. With fixed temperature differences, the latter results in natural convection

weakening when the viscosity of the PCM is increased. When the PCM is still in solid state, its viscosity is infinite, so that natural convection does not take place, but as the PCM becomes liquid after melting finishes, the viscosity falls rapidly, so that natural convection can take place.

2.3. Determination of Permeability and Inertia Factor

By employing data fitting technology, Calmidi and Mahajan (2000) obtained the empirical formula for permeability and inertial factor calculations of metal foams. Since their results showed good agreement with test data, this Chapter has employed their formula, with Eq. (7) showing permeability and Eq. (8) showing inertial factor respectively:

$$\frac{K}{{d_p}^2} = 0.00073(1-\varepsilon)^{-0.224}\left(\frac{d_f}{d_p}\right)^{-1.11} \tag{7}$$

$$C_f = 0.00212(1-\varepsilon)^{-0.132}\left(\frac{d_f}{d_p}\right)^{-1.63} \tag{8}$$

Here, d_p denotes the equivalent diameter of metal foam cells, which can be calculated if knowing the pore density: d_p = 0.0254 m/pore density. Pore density is measured in ppi (pores per inch: 1 inch = 2.54 cm). d_f denotes the equivalent diameter of metal foam fibres, calculated from

$$\frac{d_f}{d_p} = 1.18\sqrt{\frac{1-\varepsilon}{3\pi}}\left(\frac{1}{1-e^{-(1-\varepsilon)/0.04}}\right) \tag{9}$$

Calmidi (1998). To give more accurate results, Eq. (9) has taken into account the non-circular shape of metal fibres by introducing a shape factor.

3. HEAT TRANSFER

3.1. Equations of Convective Heat Transfer

In order to cope with the phase change heat transfer problem, the Enthalpy Method has been employed in this study. The relationship between PCM enthalpy function $H_f(x,y,t)$ and temperature $T_f(x,y,t)$ is given by:

$$T_f = \begin{cases} \dfrac{H_f}{C_{pf}}, & H_f \in (-\infty, C_{pf}T_m) \\ T_m, & H_f \in [C_{pf}T_m, C_{pf}T_m + H_L] \\ \dfrac{H_f - H_L}{C_{pf}}, & H_f \in (C_{pf}T_m + H_L, +\infty) \end{cases} \tag{10}$$

The Energy Equation for the metal foam (Tian and Zhao, 2011a) is given by:

$$\begin{aligned} \langle \rho_s \rangle C_{ps} \frac{\partial \langle T_s(x,y,t) \rangle}{\partial t} &= \left\langle \nabla \bullet \left[k_{se} \nabla \langle T_s(x,y,t) \rangle \right] \right\rangle \\ &- h_{sf} a_{sf} \left[\langle T_s(x,y,t) \rangle - \langle T_f(x,y,t) \rangle \right] \end{aligned} \tag{11}$$

With the enthalpy method being used in the present Chapter, the Energy Equation for the PCM is given by:

$$\begin{aligned} &\frac{\partial \langle H_f(x,y,t) \rangle}{\partial t} + \langle \rho_f \rangle C_{pf} \mathbf{V} \bullet \nabla \langle T_f(x,y,t) \rangle = \\ &\left\langle \nabla \bullet \left[k_{fe} \nabla \langle T_f(x,y,t) \rangle \right] \right\rangle + h_{sf} a_{sf} \left[\langle T_s(x,y,t) \rangle - \langle T_f(x,y,t) \rangle \right] \end{aligned} \tag{12}$$

Here, k_{se} denotes effective thermal conductivity of the metal foam, k_{fe} denotes effective thermal conductivity of the PCM, h_{sf} denotes inter-phase heat transfer coefficient between metal ligaments and PCM, and a_{sf} is specific surface area of the metal foam.

Under the Cartesian coordinate system, the above Energy Equations for the metal foam and the PCM are given by Eqs. (13) and (14) respectively:

$$\rho_s C_{ps} (1-\varepsilon) \frac{\partial T_s}{\partial t} = k_{se} \left(\frac{\partial^2 T_s}{\partial x^2} + \frac{\partial^2 T_s}{\partial y^2} \right) - h_{sf} a_{sf} \left[T_s - T_f \right] \tag{13}$$

$$\varepsilon\frac{\partial H_f}{\partial t}+\rho_f C_{pf}\varepsilon\left(u\frac{\partial T_f}{\partial x}+v\frac{\partial T_f}{\partial y}\right)=k_{fe}\left(\frac{\partial^2 T_f}{\partial x^2}+\frac{\partial^2 T_f}{\partial y^2}\right)+h_{sf}a_{sf}\left[T_s-T_f\right] \tag{14}$$

3.2. Determination of Effective Thermal Conductivity, Surface Area Density and Inter-phase Heat Transfer Coefficient

Calmidi and Mahajan (2000) presented a 2D simplified model of effective thermal conductivity for metal foams, which gave good agreement with test data. However the real microstructures in metal foams are three-dimensional, and therefore a 3D model is preferred in order to get improved accuracy. In this Chapter, a 3D structured model presented by Boomsma and Poulikakos (2001) has been used to deal with the effective thermal conductivity of metal foams. The tetrakaidecahedron was used in their model to approximate metal foam cells, because that is the polyhedron with the minimal surface energy – this is relevant because metal foam cells tend to shrink to the minimal surface when being manufactured by foaming processes. The tetrakaidecahedron is a fourteen-face polyhedron comprising six squares and eight hexagons, shown in Figure 2. By using such a polyhedron approximation, Boomsma and Poulikakos (2011) obtained good agreement between model predictions and experimental data on metal foams with porosities from 88% to 98%. Their model is shown in Eq. (15):

$$k_e=\frac{\sqrt{2}}{2\left(R_A+R_B+R_C+R_D\right)} \tag{15a}$$

$$R_A=\frac{4\lambda}{\left(2e^2+\pi\lambda(1-e)\right)k_s+\left(4-2e^2-\pi\lambda(1-e)\right)k_f} \tag{15b}$$

$$R_B=\frac{\left(e-2\lambda\right)^2}{\left(e-2\lambda\right)e^2k_s+\left(2e-4\lambda-(e-2\lambda)e^2\right)k_f} \tag{15c}$$

$$R_C=\frac{\left(\sqrt{2}-2e\right)^2}{2\pi\lambda^2\left(1-2e\sqrt{2}\right)k_s+2\left(\sqrt{2}-2e-\pi\lambda^2\left(1-2e\sqrt{2}\right)\right)k_f} \tag{15d}$$

$$R_D=\frac{2e}{e^2k_s+\left(4-e^2\right)k_f} \tag{15e}$$

$$\lambda = \sqrt{\frac{\sqrt{2}\left(2-(5/8)e^3\sqrt{2}-2\varepsilon\right)}{\pi\left(3-4e\sqrt{2}-e\right)}} \tag{15f}$$

$$e = 0.339 \tag{15g}$$

In Eqs. (15a) to (15g), R_A, R_B, R_C and R_D are the calculated thermal resistances of four different layers inside a tetrakaidecahedron cell. The effective thermal conductivity k_e is a result of these four layers being placed in parallel. k_{se} and k_{fe}, which are two important parameters in Eq. (13) and Eq. (14), can be also calculated by assigning $k_f = 0$ and $k_s = 0$ in Eq. (15) respectively.

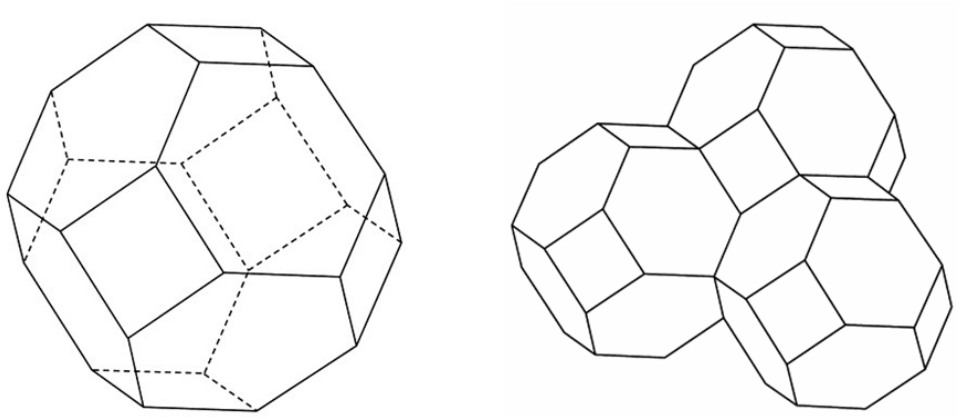

(a) A single tetrakaidecahedron; (b) Three tetrakaidecahedrons lapped together

Figure 2. Tetrakaidecahedron (Fourie and Du Plessis, 2002).

The surface area density of metal foams a_{sf} is defined as the total surface area (m^2) of metal fibres within unit volume of metal foam matrix (m^3), and it can be obtained by assuming that all metal fibres have an ideal cylindrical shape (a shape factor was also introduced by Calmidi and Mahajan (2000) to consider the non-circularity):

$$a_{sf} = \frac{3\pi d_f\left(1-e^{-\left((1-\varepsilon)/0.04\right)}\right)}{\left(0.59d_p\right)^2} \tag{16}$$

h_{sf} represents the inter-phase heat transfer coefficient between the metal foam struts and PCM. Because the metal foam struts were assumed to have the shape of cylinders, its

value is approximately calculated by the empirical formulae for the flow across a bank of cylinders (Zukauskas, 1987):

$$Nu_{sf} = \frac{h_{sf} d}{k_f} = 0.76 \mathrm{Re}_d^{0.4} \mathrm{Pr}^{0.37}, \left(1 \le \mathrm{Re}_d \le 40\right) \tag{17a}$$

$$Nu_{sf} = \frac{h_{sf} d}{k_f} = 0.52 \mathrm{Re}_d^{0.5} \mathrm{Pr}^{0.37}, \left(40 \le \mathrm{Re}_d \le 1000\right) \tag{17b}$$

$$Nu_{sf} = \frac{h_{sf} d}{k_f} = 0.26 \mathrm{Re}_d^{0.6} \mathrm{Pr}^{0.37}, \left(1000 \le \mathrm{Re}_d \le 2 \times 10^5\right) \tag{17c}$$

Details of the derivation for other parameters are given in Calmidi (1998).

3.3. Phase Field Model for Moving Boundaries

It is mathematically difficult to trace the moving boundaries for phase change phenomena. Apart from the Enthalpy Method mentioned in Section 3.1, Phase Field Model (Han et al., 2012) has recently been tested in phase change heat diffusion in metal foams.

To simulate a heat diffusion controlled phase change process, the diffusion equations are usually used for the bulk whilst the boundary conditions are specified for the moving phase change boundaries. For a general melting problem of a pure material, the governing equations in domain Ω are given (Provatas and Elder, 2010):

$$\rho c_v \dot{T} = k \nabla^2 T \quad \text{in } \Omega \tag{18}$$

$$\Delta h_m \rho v_n = -k \left[\nabla T \cdot n\right] \quad \text{on } \Gamma \tag{19}$$

$$T = T_m - \frac{\sigma}{s}(\hat{K} + \alpha v_n) \quad \text{on } \Gamma \tag{20}$$

Here, Ω is the computational domain of the solid and liquid phases, Γ is the interface between the solid and liquid phase, T is the system temperature, T_m is the melting temperature, k is the system thermal conductivity, Δh_m is the latent heat, v_n is the normal velocity on the interface, σ is the surface tension, s is the entropy density difference between phases, $\hat{K}$ is curvature of the interface, α is the relaxation scaling, ρ is the density of the system (ρ_l for liquid phase and ρ_s for solid phase) and c_v is the specific heat capacity of the system (c_{vl} for liquid phase and c_{vs} for solid phase).

Eq. (18) is the heat diffusion equation for both liquid and solid phases. Eq. (19) is known as the Stefan condition for free boundary problems. It is described by the local velocity of a moving boundary as a function of temperature gradient across phases. This relationship derives from the energy conservation at the interface. Eq. (20) is known as Gibbs-Thomson relation.

For a phase change problem which involves only latent heat, the phase change process is classified as a typical first-order phase transformation in Phase Field Theory. On the basis of Landau theory (Provatas and Elder, 2010), an order parameter is introduced to separate ordered phases and disordered phases. In phase transformation, ordered phases are often distinguished from disordered phases by a decreased number of geometric symmetries (Provatas and Elder, 2010). For the case of melting, the liquid phase is considered to be disordered (symmetric) whilst the solid phase is considered to be ordered (asymmetric). In Landau theory, the order parameter η acts as a state variable, and in the study by Han et al. (2012), the liquid phase was defined by $\eta = 1$ and the solid phase was defined by $\eta = -1$. They called the set of values of η over the whole computational domain as the phase field. According to Landau theory, the free energy can be written as a function of order parameter using Taylor expansion (Provatas and Elder, 2010):

$$f(\eta) = f(T, \eta = 0) + \sum_{n=2}^{M} \frac{a_n(T)}{n} \eta^n \tag{21}$$

The order parameter is a non-conserved quantity in melting process (Provatas and Elder, 2010), for first-order phase transformation the simplest Langevin equation therefore gives:

$$\frac{\partial \eta}{\partial t} = -M \frac{\partial F(\eta, T)}{\partial \eta} \equiv M \left(W_0 \nabla^2 \eta - \frac{\partial f(\eta, T)}{\partial \eta} \right) \tag{22}$$

Here, M is a mobility which will be determined for specific problems, W_0 is a constant which relates to surface tension. Substituting Eq. (21) into Eq. (22), the one-dimensional melting problem for a pure material is given by (Provatas and Elder, 2010):

$$\alpha \varepsilon^2 \frac{d\eta}{dt} = \varepsilon^2 \frac{d^2 \eta}{dy^2} - \frac{1}{2}\left(\eta^3 - \eta\right) + \frac{\varepsilon s}{2\sigma}\left(T - T_m\right)\left(1 - \eta^2\right). \tag{23}$$

Thus, a modified heat diffusion equation, earlier shown in Eq. (18), is given by

$$\rho c_v \frac{dT}{dt} = \frac{d}{dy}(k\frac{dT}{dy}) - \frac{1}{2}\Delta h_m \rho \frac{d\eta}{dt} \ , \tag{24}$$

Here, Δh_m is latent heat of fusion and ε is the thickness of the interface. Eqs. (23) and (24) are alterative governing equations using phase field model.

By using phase field method, volume expansion in melting process can be taken into account by introducing another phase field: η_1. The variation of the density of the PCM from liquid phase to solid phase leads to a volume expansion during melting. As the volume expansion only occurs in the melting zone (the interface between liquid and solid phase), in which the values of η vary from –1 to +1 ($-1 \le \eta \le +1$), the PCM not in the melting zone will only undergo a coordinate shift. The objective therefore becomes to find how much the PCM expands during a specific time.

Figure 3(a) shows the liquid phase, solid phase and 'ghost phase', with two fronts: melting front and sample boundary. The ghost phase does not actually exist, and is just a virtual domain to consider volume change. During a melting process, melting front will move to the left, whilst the sample boundary will move to the right due to volume expansion. Figure 3(b) gives the initial boundary conditions for order parameter η and η_1: η is set to –1 to specify solid phase, and is set to +1 for other phases (the solid line); η_1 is set to +1 for the solid and liquid phases (the whole PCM sample), whilst it is set to 0 for the ghost phase (the dashed line). Unlike the expression of phase field η which was derived from the free energy equation, the evolution equation of η_1 conforms to the kinetic equation:

$$\frac{d\eta_1}{dt} = v_e \frac{d\eta_1}{dy} + D_e \frac{d^2\eta_1}{dy^2}. \tag{25}$$

The first term on the right hand side of Eq. (25) represents the front migration rate with its corresponding velocity v_e. The second term ensures a numerical stability of the system and gives the front a finite and small width. The value of D_e is empirical and is assumed to be large enough to stabilize the system but small enough to be able to provide a small width. v_e is the velocity of PCMs sample boundary migration due to volume expansion. The velocity v_e is given by the Mass Conservation Law:

$$v_e = \left(\frac{\rho_s - \rho_l}{\rho_l} \right) \left(\frac{r_{melt}}{r_{boundary}} \right) v_{melt} \ , \tag{26}$$

Here, r_{melt} and $r_{boundary}$ denote the positions when $\eta = 0$ and $\eta_1 = 0.5$, respectively. To obtain v_{melt} which cannot be calculated from equations above, an average velocity during a period Δt is used: $v_{melt}(t) = r_{melt}(t)\Big|_t^{t+\Delta t} / \Delta t$. Eq. (24) is modified to consider volume expansion and varied physical properties in solid and liquid phases:

$$\frac{dT}{dt} = \frac{1}{\rho(\eta) c_v(\eta)} \frac{d}{dy} (k(\eta) \frac{dT}{dy}) \eta_1 - \frac{1}{2} \frac{\Delta h_m}{c_v(\eta)} \frac{d\eta}{dt} - v_e \left(\frac{\eta + 1}{2} \right) \frac{dT}{dy} \tag{27a}$$

$$\rho(\eta) = \left(\frac{\rho_l - \rho_s}{2} \right) \eta + \left(\frac{\rho_l + \rho_s}{2} \right) \tag{27b}$$

$$c_v(\eta) = \left(\frac{c_{vl} - c_{vs}}{2} \right) \eta + \left(\frac{c_{vl} + c_{vs}}{2} \right) \tag{27c}$$

$$k(\eta) = \left(\frac{k_l - k_s}{2} \right) \eta + \left(\frac{k_l + k_s}{2} \right) \tag{27d}$$

Eq. (27a) describes that the energy during melting is balanced in three ways: heat diffusion (the first term on the right hand side), latent heat (the second term on the right hand side) and liquid domain shift (the third term on the right hand side). Eqs. (27b)–(27d) indicate linear relationships between different physical properties (density, specific heat capacity and heat conductivity) and order parameter η.

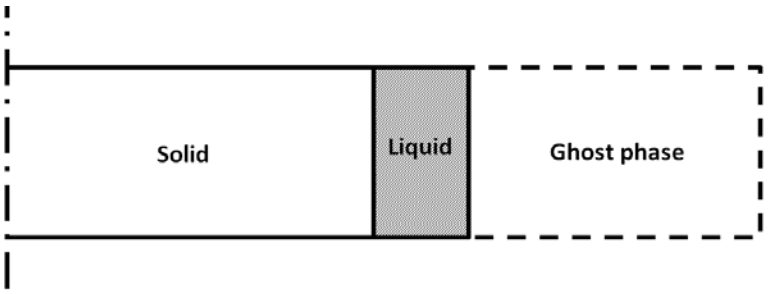

(a) Three phases;

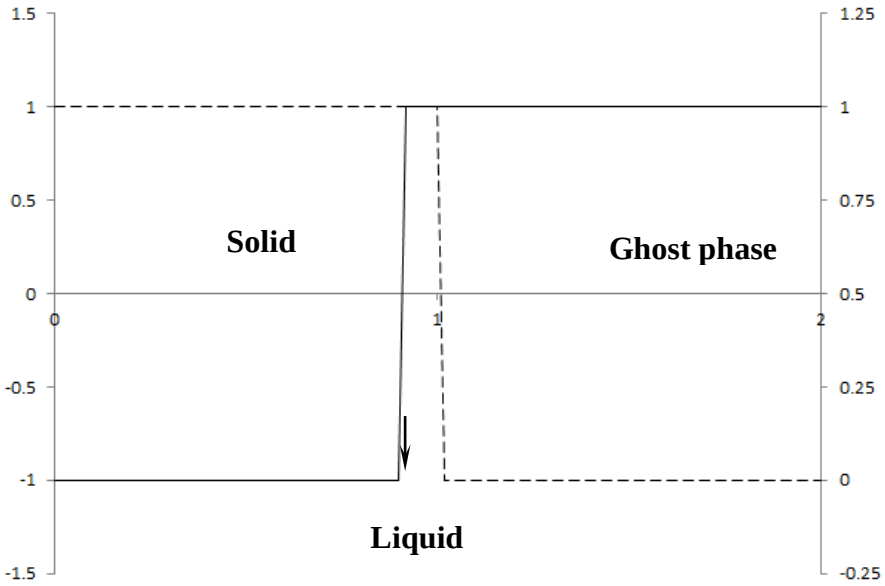

(b) Initial conditions for three phases

Figure 3. Volume expansion during melting.

4. APPLICATIONS

This section focuses on practical applications of high porosity cellular metal foams in enhancing heat transfer for Thermal Energy Storage (TES). Section 4.1 discusses metal foam-embedded PCM system (Zhao et al., 2010; Tian and Zhao, 2011a). Section 4.2 discusses metal foam-enhanced cascaded thermal energy storage (Tian et al., 2012; Tian and Zhao, 2013).

The metal foam-embedded PCM system is numerically and experimentally investigated, with natural convection and temperature profiles during melting being examined. Metal-foam samples of different porosities and pore densities will be analysed and compared, and a comparison between them and the pure PCM sample will also be given. In addition, the Phase Field Model, as a new numerical method to track the moving phase-change interface, will be presented and compared with both experimental data and other models.

Metal foam-enhanced cascaded thermal energy storage is investigated by numerical simulations, with the results being verified by experiment. Three cases will be compared: single-stage storage, cascaded storage and metal foam-enhanced cascaded storage. An exergy analysis will also be presented.

4.1. Heat Transfer Enhancement of PCMs by Metal Foams

4.1.1. Physical Problem

As shown in Figure 4, the PCM RT58 (provider: RUBITHERM®) is impregnated into a piece of rectangular copper foam. The lengths of the sample are L_1 in x-direction and L_2 in y-direction. The PCM and metal foam are heated from the bottom side by a constant heat flux q_w, whilst losing heat through the left, right and top boundary. h_1, h_2 and h_3 are heat loss coefficients. The PCMs and metal foams used are listed in Table 1 and 2, respectively.

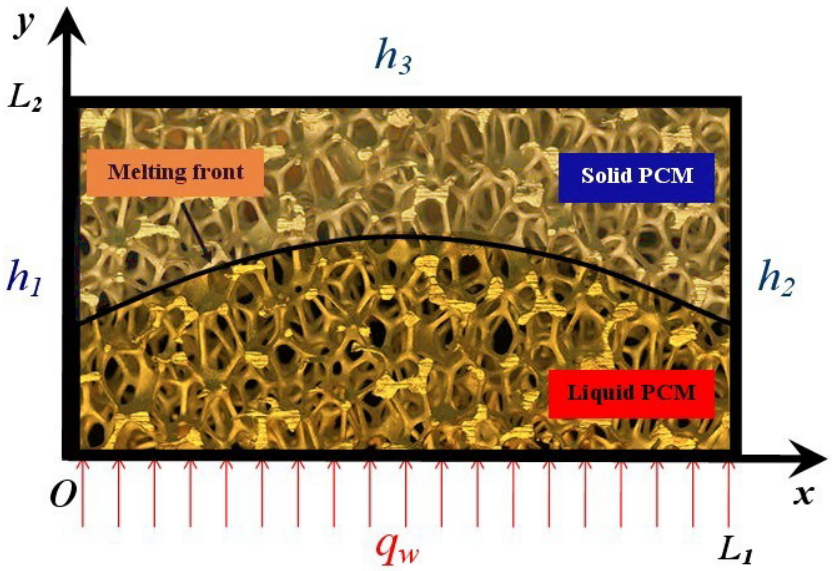

Figure 4. Copper foam embedded with PCM.

Table 1 Thermal properties of RT58, Rubitherm®, Germany.

PCM	Density (kg/m^3)	Melting temperature (℃)	Latent heat per kg (kJ/kg)	Latent heat per m^3 (MJ/m^3)	Specific heat (kJ/kg ℃)	Thermal conductivity (W/ m K)	Thermal expansion coefficient (K^{-1})	Dynamic viscosity (Pa s)
RT 58	880	48-62	181	159	2.1	0.20	1.1×10^{-4}	0.0269

Table 2 Metal foam properties.

Properties	Porosity ε	Pore density	k_s in Eq. (30)
Sample A	0.95 (95%)	10ppi	350 W/(m K)
Sample B	0.95 (95%)	30ppi	350 W/(m K)
Sample C	0.85 (85%)	30ppi	350 W/(m K)

4.1.2. Experimental Test-rig and Results

The experiment setup is shown schematically in Figure 5. The test section comprises a piece of rectangular metal foam (copper foam with the dimension of 200×120×25 mm) with paraffin wax RT58 embedded in it. The metal foam was sintered onto a thin copper plate from the bottom side for better thermal contact. Attached to the copper plate was an electrical heater which is made of flexible silicon with adjustable heat flux, providing continuous and uniform heat flux for the PCM and metal foam. The heater input power could be precisely controlled and measured by a Variac and an electrical power meter (Hameg HM8115-2, accuracy ±0.5%). This allowed the heat flux used in the test to be calculated through dividing the input power by the surface area of the copper plate.

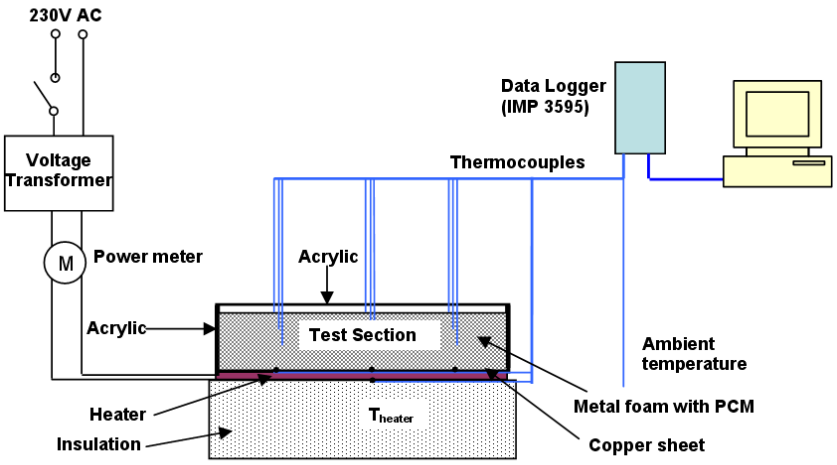

Figure 5. Experimental rig.

In this test, nine thermocouples (accuracy ±0.1ºC) were placed at different locations inside the PCM to monitor the transient temperature variation (y = 8 mm, 16 mm and 24 mm respectively, where y is the vertical coordinate in the computational domain, namely the distance between different locations and heating plate. 3 thermocouples were used for each place to get more reliable readings). Three thermocouples were placed on the copper plate to record the plate temperatures (y = 0 mm). Although perfect insulation could not be guaranteed in the test, the underneath of the heating surface was insulated with Armflex insulation material and other surfaces were insulated by acrylic sheets which were transparent for observation during the tests. The temperatures and the input power were automatically recorded by a data acquisition system. From the previous work by Zhao et al. (2010), the overall experimental error was estimated at 6.67%.

The comparison between the pure RT58 sample and two metal-foam samples during melting process (charging) is shown in Figure 6 ($\Delta T = T_{y=0\,mm} - T_{y=8\,mm}$), from which it can be seen that the heat transfer enhancement in PCM caused by metal foams on solid/liquid phase change heat transfer zone is significant, especially at the solid zone. The heat transfer rate can be enhanced by 5–20 times. When the PCM starts melting, natural convection takes place and it improves the heat transfer performance, thereby reducing the temperature difference between the wall and PCM. Even so, the addition of the metal

foam can increase the overall heat transfer rate 3-10 times (depending on the metal foam structures) during the melting process (two-phase zone) and the liquid zone. It can also be concluded from Figure 6 that the metal foam sample with larger relative density (namely smaller porosity) has better heat transfer performance than the one with smaller relative density. This is reasonable because larger relative density means larger percentage of metal skeleton, which is helpful for transferring heat from heating plate to the PCM more effectively.

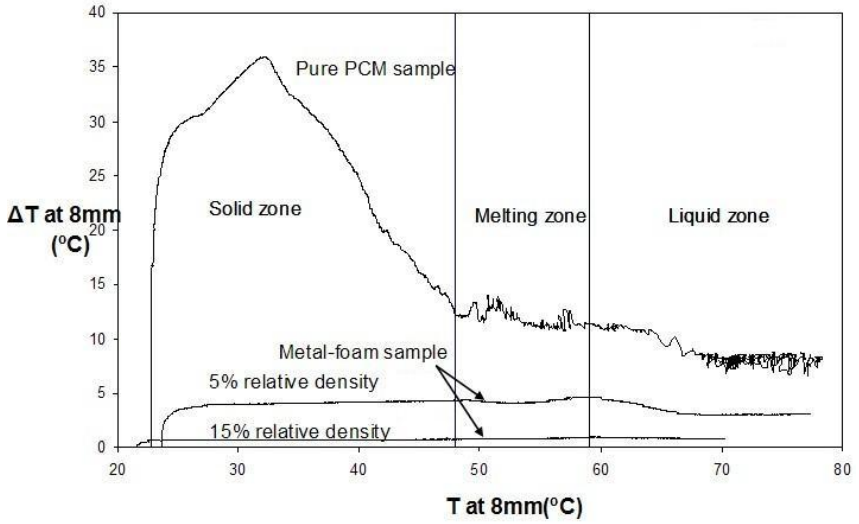

Figure 6. A comparison between the pure PCM sample and metal-foam samples.

4.1.3. Comparison between Experimental Data and Numerical Results

The numerical results and the corresponding experimental data are compared in Figure 7 for y = 0 and 8 mm. Both numerical results and experimental data show that the PCM begins to melt around t = 1200s and finish phase change around t = 4000s. There is good agreement between numerical results and experimental data, and the most probable reason for the small discrepancies between them is that it has been assumed in the model that the PCM has a fixed melting point, similarly to crystal materials. In practice, is important to note that, RT58 melts in a temperature range of 48-62ºC (according to RUBITHERM®).

As shown in Figure 7, the temperatures of RT58 increase more slowly after melting begins, because the heat provided is mainly used for phase change rather than increasing sensible heat. After the state of RT58 has become fully liquid (when temperatures are higher than 62ºC), its temperatures begin to increase more rapidly again, because the heat provided is now all used for increasing sensible heat of the PCM.

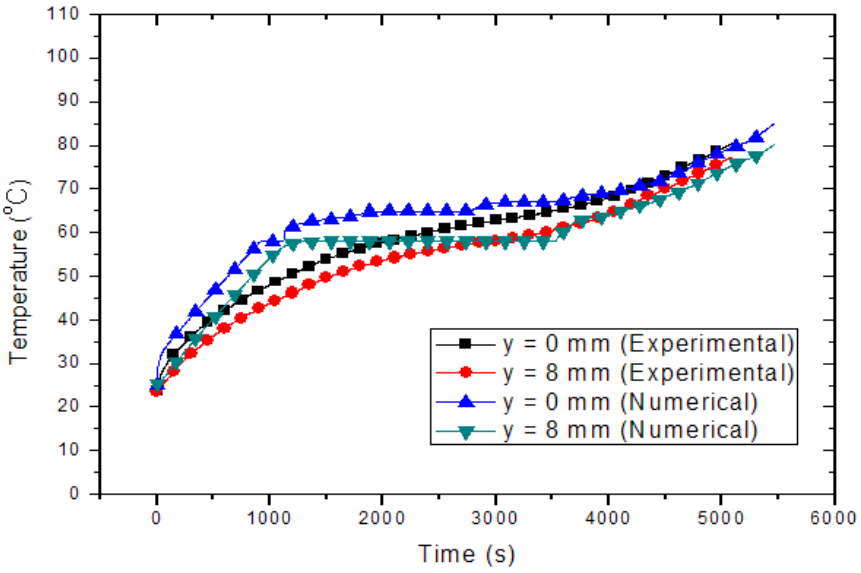

Figure 7. A comparison between numerical results and experimental data.

4.1.4. Natural Convection

Figure 8 presents the buoyancy-driven velocities in metal-foam-embedded PCM during phase change. It can be seen that two symmetrical eddies (anti-clockwise on the left, and clockwise on the right) were formed when natural convection commenced. The PCM near the symmetrical plane (x = 0.1) tended to move upward, whilst the PCM on the left/right side tended to move downward. This is because the PCM became cooler when losing heat to atmosphere on the left/right side; however, whilst it kept relatively warm on the symmetrical plane (thermally insulated). When t = 1108.3 s, only a small part of PCM has been melted and starts natural convection. As time increases, more and more PCM is being melted. When t = 5859.0 s, PCM has been fully melted.

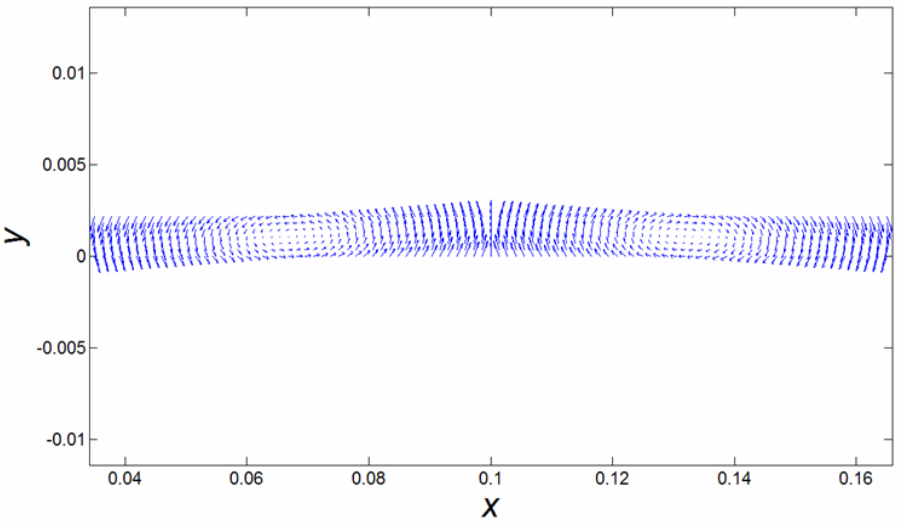

(a) (t = 1108.3 s);

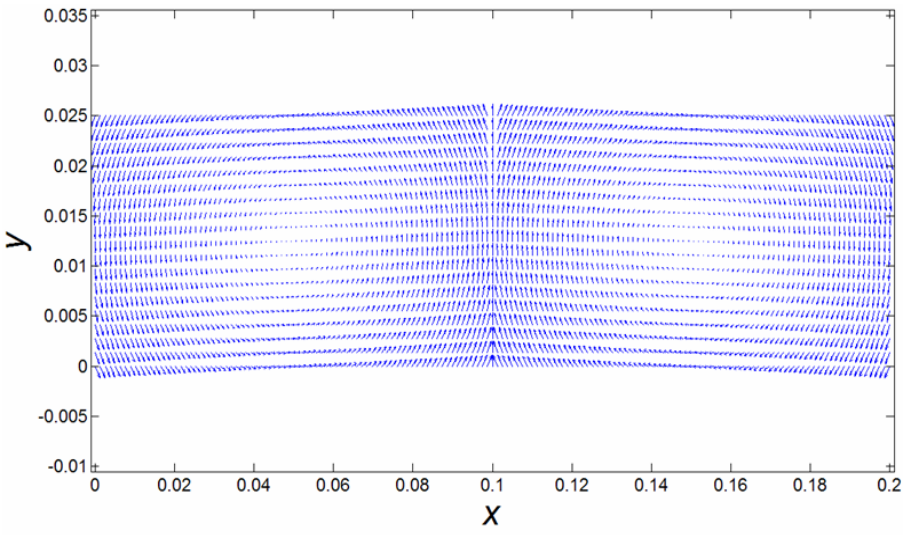

(b) (t = 5859.0 s).

Figure 8. Velocity profile of natural convection.

The occurrence of natural convection is beneficial to heat transfer enhancement. However, the numerical investigation indicates that buoyancy-driven velocities are rather low, with an order of magnitude of 10^{-5} m/s. At first sight, the result may seem surprising, but it is believed to be reasonable after a careful semi-quantitative analysis. The buoyancy force term $\rho_f g\beta\Delta T$, has an order of magnitude of 10^1, whilst the amplification coefficient μ_f / K in the primary drag force term, has an order of magnitude of 10^6.

According to the equilibrium condition of forces shown in Eq. (6), the drag force should bear similar order of magnitude to the buoyancy force, consequently u should have an order of magnitude of 10^{-5}. Paraffin wax RT 58 used in this study has a high dynamic viscosity of 0.0269 Pa·s (1000 times bigger than air) and a low thermal expansion coefficient of $1.1*10^{-4}$ K^{-1} (30 times smaller than air) [13]. These two factors made natural convection too weak to produce dominant influence on heat transfer. Additional cases have also been examined for lower viscosities, with all other parameters remaining unchanged. They are shown in Figure 9 (Tian and Zhao, 2011b), with the points 1–8 representing the viscosity of μ_f, $0.1\mu_f$, $0.01\mu_f$, $0.001\mu_f$, $0.0002\mu_f$, $0.0001\mu_f$, $0.00002\mu_f$ and $0.00001\mu_f$, respectively. As seen in Figure 9, natural convection becomes stronger when decreasing viscosity, which significantly enhances heat transfer in PCM.

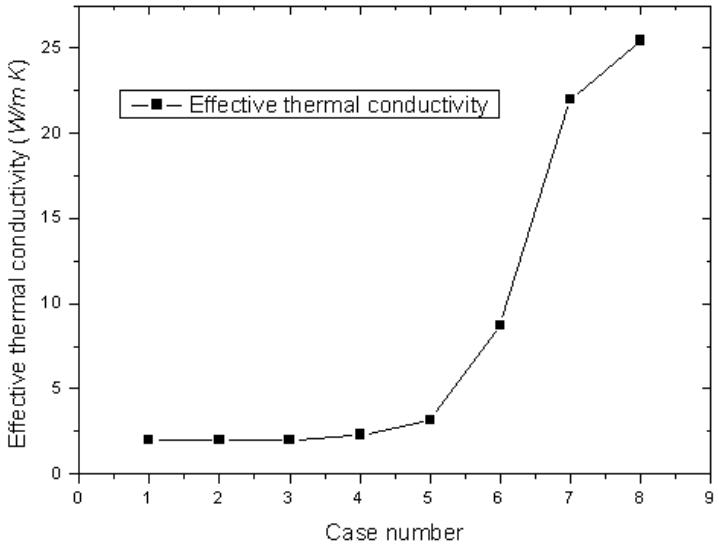

Figure 9. The effect of the PCM viscosity on natural convection.

4.1.5. Temperature Profiles

Figures 10(a) – (d) show the evolution of temperature profiles for the metal-foam sample with 95% porosity and 10 ppi during melting process. Fig. 10(a) shows its temperature profiles at t = 976.5 s. At this time, the maximum temperature of the PCM in the whole region is 57ºC which is still just below melting point (58ºC). When t = 1108.3 s, a small part of PCM near bottom side has been heated up to melting point (58ºC) and begins to melt gradually, as shown by those isotherms in Fig. 10(b). It also shows that the left and

right parts of PCMs near bottom side have not yet begun to melt, because the PCM here is losing heat to atmosphere through the left and right boundary and consequently has not acquired enough heat to before melting.

As time increases, the melting front gradually moves upwards, meaning more and more of the PCM is being melted, as shown in Fig. 10(c). The PCM temperature profiles when t = 5859.0s are shown in Fig. 10(d). At this time, all of the PCM has been fully heated into liquid state, with the minimum and maximum temperatures being 72ºC and 92ºC.

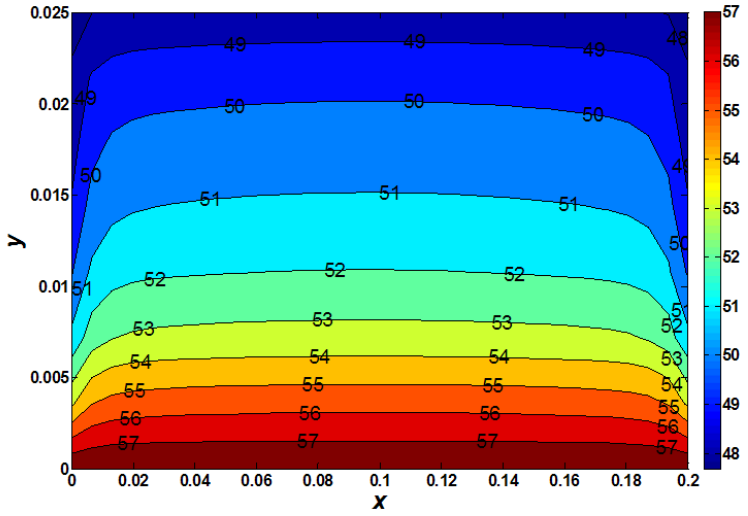

(a) t = 976.5 s.

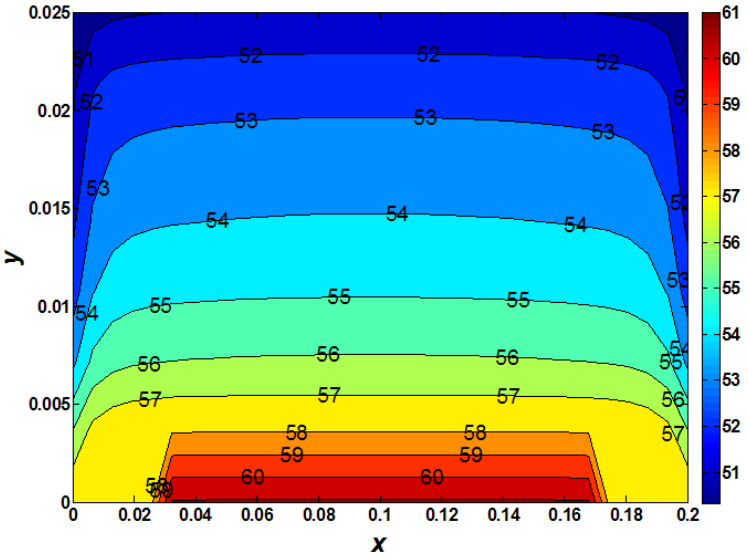

(b) t =1108.3 s.

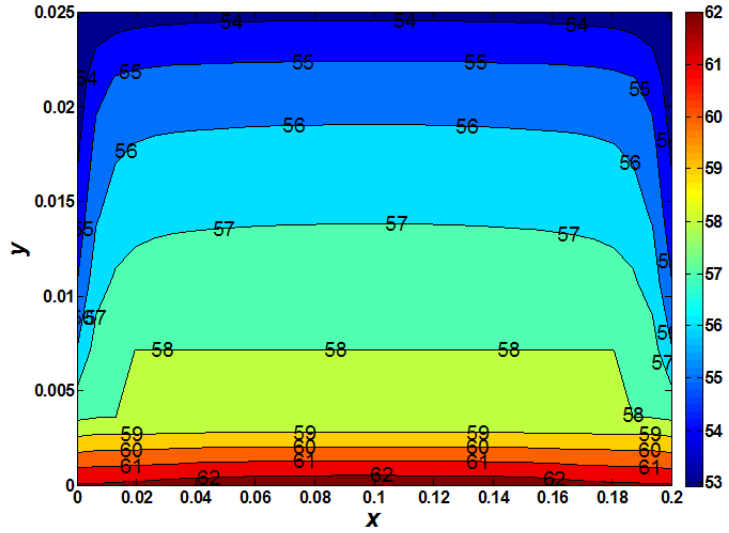

(c) t = 1318.3 *s*.

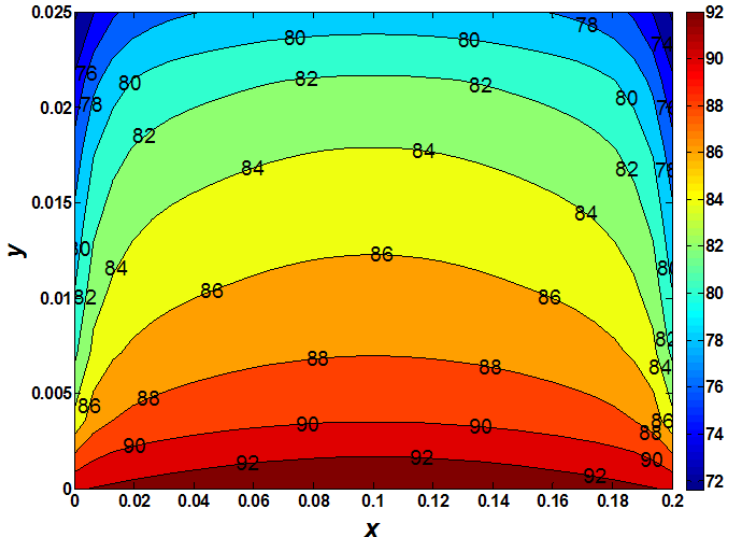

(d) t = 5859.0 *s*.

Figure 10. Temperature profiles.

4.1.6. Effects of Metal Foam Microstructures

Figure 11(a) gives the equivalent thermal conductivities for three metal-foam samples and pure PCM. It indicates that all three metal-foam samples have better heat transfer performance (3-10 times higher on average) than the pure PCM sample. The metal foams with larger pore density (measured in ppi) and smaller porosity (%) exhibit even better results for heat transfer enhancement, because they have larger surface area density and higher volume percentage of metal structures, which are both beneficial to heat transfer. The enhancement effect by metal foams is significantly strong (10–50 times higher), especially in the solid region, where heat conduction dominates. However, their enhancement effect is weakened in the liquid region (2–10 times), due to metal foams suppressing natural convection.

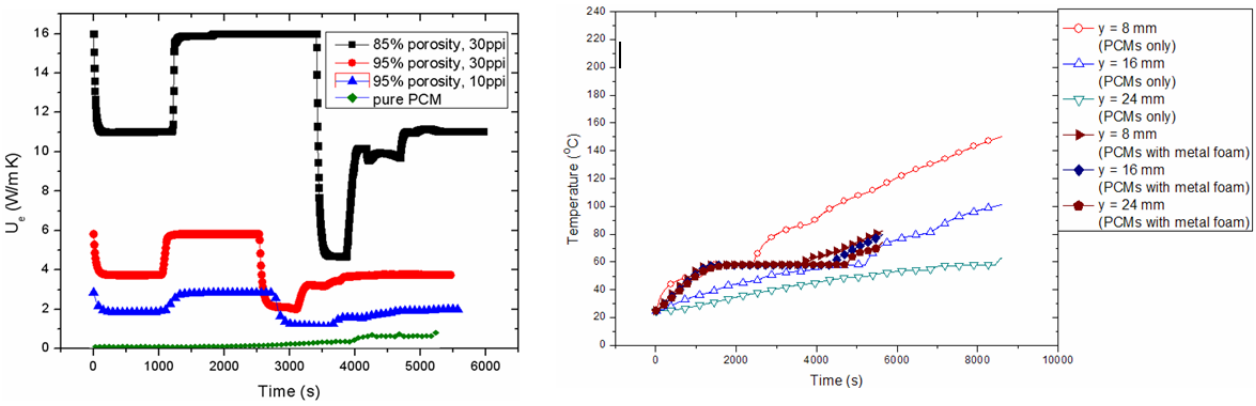

(a) Metal-foam samples vs. pure PCM; (b) Heat conduction only.

Figure 11. Metal-foam samples vs. pure PCM**.**

In order to reveal the enhancement effect of metal foams by heat conduction only, Fig. 11(b) makes the comparison between the metal-foam sample (95% porosity and 10 ppi) and pure PCM, with natural convection eliminated during simulation (Tian and Zhao, 2009). It can be seen that the use of metal foams considerably reduced the temperature differences in PCM at both solid and liquid region, significantly promoting the heat transfer performance (smaller temperature differences imply higher equivalent thermal conductivities, when the heat flux is fixed).

4.1.7. Results from Phase Field Method

The Phase Field Model is a newly developing method to tackle the moving boundaries during phase change, and it has been tested in metal foam-embedded PCM systems. By employing the Phase Field Method, Han et al. (2012) obtained the temperature evolution over time for two different positions inside the PCM. Their model results are compared with the corresponding experimental data, shown in Figure 12. The discrete symbols are experimental data while the lines are model predictions. The melting zone can be observed in Figure 12, which ranges from 50 ^{o}C (at 1300 seconds) to 58 ^{o}C (at 3300 seconds). The model predictions achieved a better agreement with the experimental data than the previous study by Zhao et al. (2010). The main reason is that the Phase Field Model can deal with variable melting points but a fixed melting point was assumed in the study by Zhao et al. (2010). However, the model prediction from Han et al. (2012) does not fit well with the experimental data on the later stage after melting, because nature convection was neglected in their study, which usually has a significant effect on heat transfer.

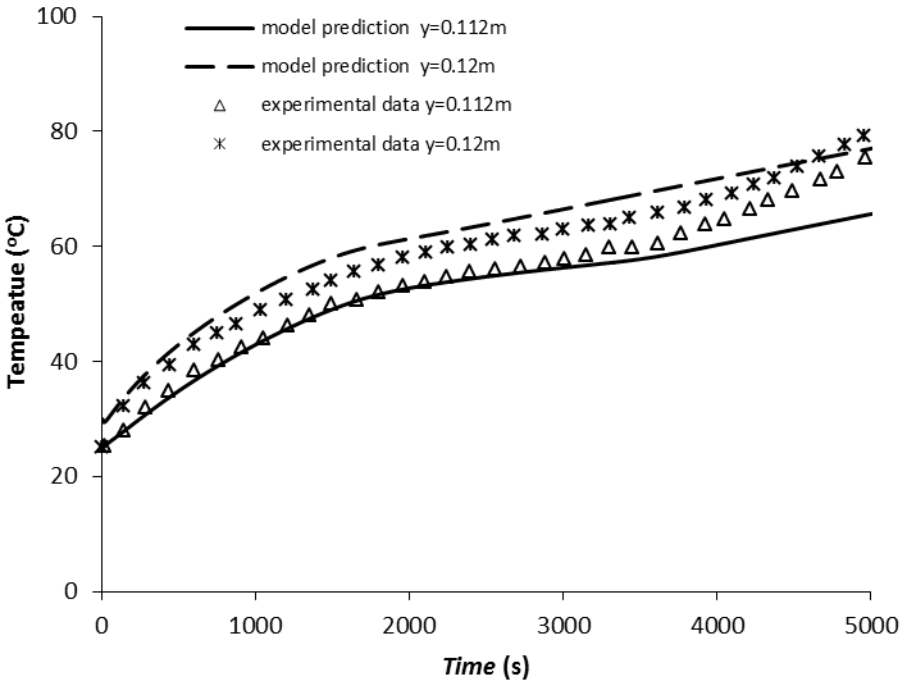

Figure 12. Model predictions (lines) compared to experimental data (discrete symbols).

4.2. Exergy Analysis of Metal Foam-enhanced Cascaded Thermal Energy Storage (MT-CTES)

Metal foam enhanced cascaded thermal energy storage will be investigated by numerical simulations in this Section. To consider the fact that not all the energy stored can be used, an exergy analysis is also presented. For simplicity, only main results are presented in this Section, and the verification of the numerical simulations is given by Tian and Zhao (2013).

4.2.1. Physical Problem

Metal Foam-enhanced Cascaded Thermal Energy Storage (MF-CTES), which are illustrated in Figures 13(a), (b) and (c), respectively. STES is formed by a single PCM. Both CTES and MF-CTES are formed by staging three PCMs along the HTF (heat transfer fluid) flow direction. CTES and MF-CTES are made of the same PCMs, with the only difference being that MF-CTES uses metal foam to enhance heat transfer. The thermo-physical properties of PCM 1, 2, 3 and 4 are listed in Table 3.

In Figure 13, H_L (kJ/kg) and T_m (℃) denote the latent heat and melting temperature, respectively; h and L denote system dimensions. The HTF enters each system from the left (inlet temperature T_{f0} = 100℃), and exits from the right with the outlet temperature $T_f(t)$ which varies with time. The melting temperature of PCM 4 (in STES) was chosen to have the average value of the melting temperatures of PCM 1, 2 and 3, so that a comparison between the three systems is justified. The initial temperatures of all three systems are equal to the ambient temperature, which is 20℃. Other parameters for the systems are given in Table 4.

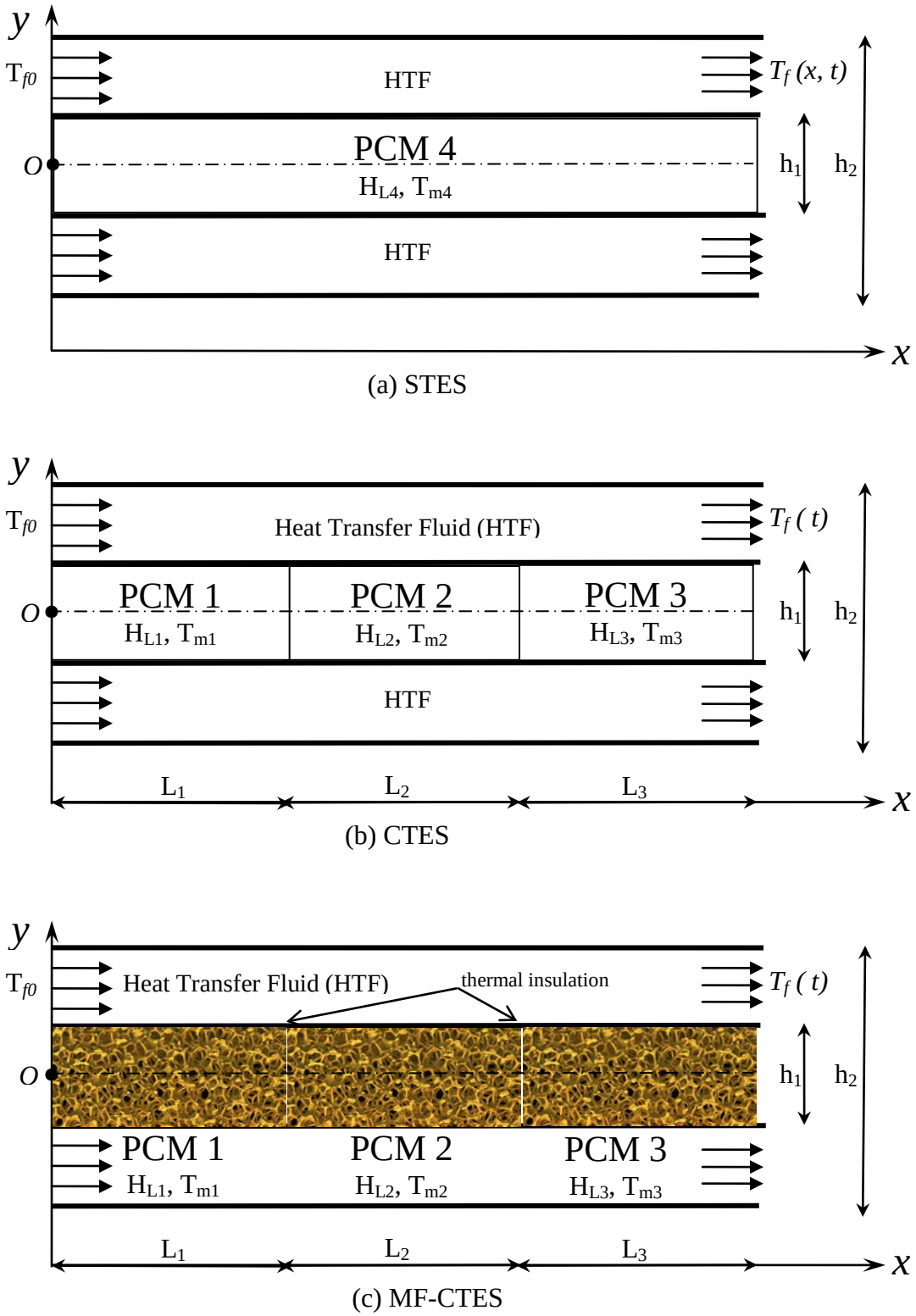

Figure 13. STES, CTES and MF-CTES.

Table 3 Thermal properties of PCMs (Rubitherm Technologies Gmbh).

PCMs	PCM 1	PCM 2	PCM 3	PCM 4
Product code (Rubitherm®)	RT31	RT50	RT82	RT55
Melting temperature (℃)	31	50	82	55
Density (kg/m^3)	880.0	880.0	880.0	880.0
Latent heat(kJ/kg)	169.0	168.0	176.0	172.0
Specific heat (kJ/kg ℃)	2.1	2.1	2.1	2.1
Thermal conductivity (W/m K)	0.2	0.2	0.2	0.2
Linear thermal expansion coefficient (K^{-1})	1.1×10^{-4}	1.1×10^{-4}	1.1×10^{-4}	1.1×10^{-4}
Kinetic viscosity (mm^2/s)	28.57	31.20	45.45	34.08
Dynamic viscosity (Pa·s)	0.0251	0.0275	0.0400	0.0300

Table 4 System parameters.

HTF properties		System dimension	
Density: ρ	1000 kg/m^3	L_1	3.5 m
Velocity: v	0.5 m/s	L_2	3.5 m
Dynamic viscosity at 50 ℃: υ	0.553×10^{-6} m^2/s	L_3	3.5 m
Prandtl number at 50 ℃: Pr	3.56	h_1	0.02 m
Specific heat: c_p	4.2 kJ/(kg ℃)	h_2	0.04 m
Thermal conductivity: λ_{HTF}	0.6 W/(m K)	Characteristic diameter	
		$d = (h_2–h_1)/2$	0.01 m
Inlet temperature: T_{f0}	100 ℃		
Ambient temperature: T_a	20 ℃		

4.2.2. Comparison of Exergy Transfer Rates among STES, CTES and MF-CTES.

Effective exergy transfer rates h_{ex} were obtained by numerical simulations for STES, CTES and MF-CTES. Figure 14 shows the comparison of h_{ex} between STES and CTES system, it can be concluded that CTES nearly always produces higher exergy transfer rate (up to 23%) than STES. It needs to be noted that CTES delivers slightly lower exergy transfer rate than STES, only when PCM 1 starts phase change and after PCM 4 finishes phase change. There are two probable reasons for this. Firstly, when PCM 1 starts its phase change, CTES had lower exergy efficiency than STES despite of CTES having slightly higher heat transfer rate than STES. Secondly, after PCM 4 finishes its phase change, the heat transfer rate of STES is higher than CTES due to the long-time delay of temperature rise (latent heat of PCM 4), but the exergy efficiency STES is much lower than CTES due to its low temperatures after phase change.

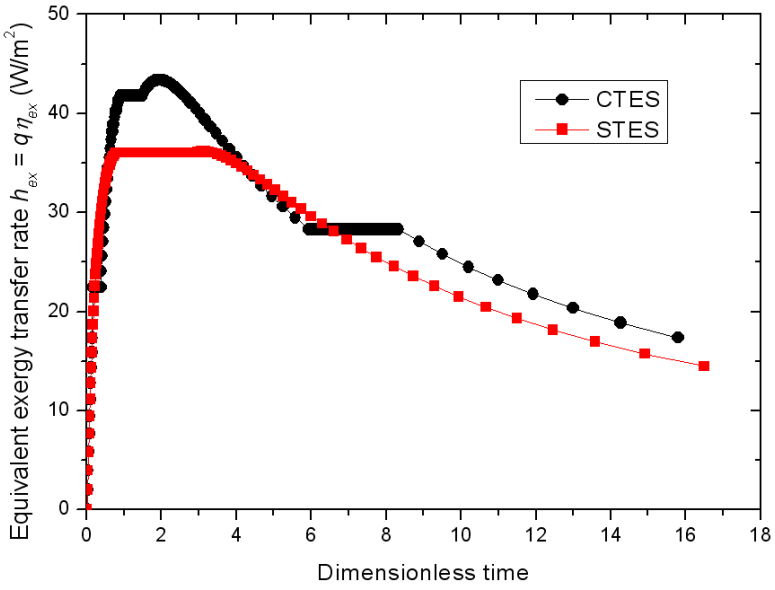

Figure 14. A comparison of h_{ex} between STES and CTES.

Figure 15 compares the effective exergy transfer rate (h_{ex}) of MF-CTES among three different copper-foam samples, indicating that Sample C has the highest h_{ex} than Sample A and B, and that all metal-foam samples have much higher h_{ex} (by 2–7 times) than CTES.

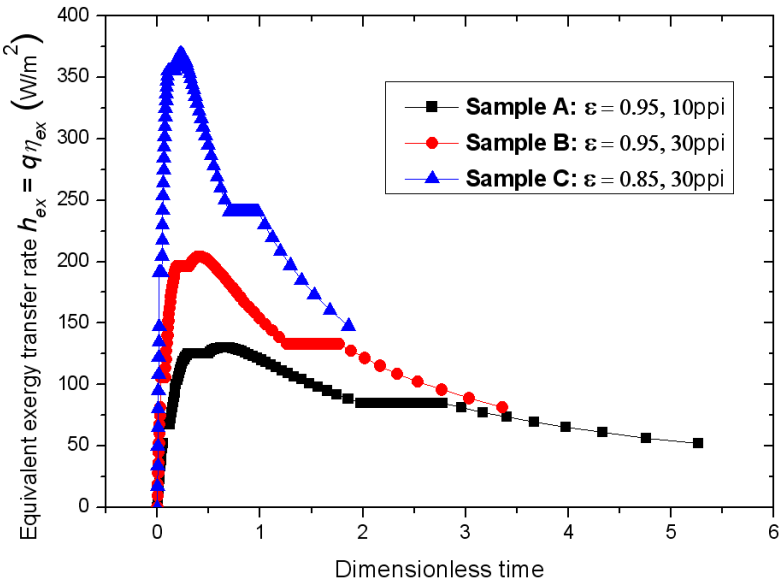

Figure 15. A comparison of h_{ex} among different metal-foam samples for MF-CTES.

In summary, CTES nearly always has higher exergy transfer rates (up to 23%) than STES; MF-CTES can further increase exergy transfer rates of CTES by 2–7 times.

CONCLUSION

Phase change convective heat transfer in high porosity cellular metal foams has been investigated, with various mathematical models being discussed and reviewed. The non-Darcy effects and buoyancy-driven natural convection in metal foams are also analysed. Finally, these models have been applied to two applications: metal foam-embedded PCM, and metal foam-enhanced cascaded TES. Through experimental and numerical investigations, metal foams have been found to improve heat transfer rate averagely by 5–10 times, and exergy transfer rate averagely by 2–7 times.

NOMENCLATURE

a_{sf}	=	specific surface area	m^{-1}
C_f	=	inertia coefficient of fluid flow in metal foams	(dimensionless)
C_p	=	specific heat at constant pressure	kJ/(kg ^oC)
C_{ps}	=	specific heat of metal at constant pressure	kJ/(kg ^oC)
C_{pf}	=	specific heat of PCM at constant pressure	kJ/(kg ^oC)
c_v	=	specific heat capacity at constant volume	kJ/(kg K)
d_f	=	equivalent diameter of metal fibre	m
d_p	=	equivalent pore size	m
e	=	length ratio of cubic juncture node to ligament	(dimensionless)
$\mathbf{g}$	=	gravity vector	m/s^2
H_L	=	latent heat	kJ/kg
h_1	=	heat transfer coefficients at the left boundary	$W/(m^2K)$
h_2	=	heat transfer coefficients at the right boundary	$W/(m^2K)$
h_3	=	heat transfer coefficients at the top boundary	$W/(m^2K)$
h_{sf}	=	interstitial heat transfer coefficient	$W/(m^2K)$
h_{ex}	=	effective exergy transfer rate	W/m^2
K	=	permeability	m^2
$\hat{K}$	=	curvature of the interface	m^{-1}
k_{fe}	=	effective thermal conductivity without metal	W/(mK)
k_{se}	=	effective thermal conductivity without fluid	W/(mK)
L_1	=	length of the PCM sample in *x*-axis	m
L_2	=	length of the PCM sample in *y*-axis	m
n	=	the normal vector on the melting interface	(dimensionless)
P	=	pressure	Pa
q_w	=	heat flux	W/m^2
s	=	entropy density	$kJ/(m^3K)$

T	=	time	s
$T(x,y,t)$	=	temperature function	^{o}C
T_{f0}	=	HTF inlet temperature	^{o}C
T_m	=	fusion temperature	^{o}C
U	=	equivalent thermal conductivity	W/(mK)
u	=	the component of the velocity **V** in x-direction	m/s
v	=	the component of the velocity **V** in y-direction	m/s
v_e	=	velocity of the external boundary	m/s
v_{melt}	=	velocity of the melting front	m/s
v_n	=	normal velocity of the melting front	m/s
V	=	velocity vector	m/s

SUBSCRIPTS

e	=	effective value
f	=	fluid (PCM)
fe	=	effective value for PCM
ref	=	reference value
s	=	metal foam
se	=	effective value for metal foam

GREEK

β	=	thermal expansion coefficient	K^{-1}
ε	=	porosity	(percentage)
λ	=	ratio of ligament radius to ligament length	(dimensionless)
η	=	order parameter for melting	(dimensionless)
η_1	=	order parameter for volume expansion	(dimensionless)

ρ	=	density	kg/m^3
σ	=	surface tension	kJ/m^2
μ_f	=	dynamic viscosity	Pa s
Ω	=	regions of solid and liquid phases	
Γ	=	melting front between solid and liquid phases	
∇	=	Laplace operator	

REFERENCES

Boomsma, K., Poulikakos, D., 2001. On the effective thermal conductivity of a three-dimensionally structured fluid-saturated metal foam. Int. J. Heat Mass Tran. 44, 827–836.

Brinkman, H.C., 1947. A calculation of the viscous force exerted by a flowing fluid on a dense swarm of particles. Appl. Sci. Res. A1, 27-34.

Calmidi, V.V., 1998. Transport Phenomena in High Porosity Metal Foams. Ph.D thesis, University of Colorado, U.S.A.

Calmidi, V.V., Mahajan, R.L., 2000. Forced convection in high porosity metal foams. J. Heat Trans.– T ASME 122, 557–565.

Forchheimer, P., 1901. Wasserbewegung durch Boden. Forsch. Ver. D. Ing. 45, 1782–1788.

Fourie, J.G., Du Plessis, J.P., 2002. Pressure drop modelling in cellular metallic foams. Chem. Eng. Sci. 57, 2781–2789.

Han, X.X., Tian, Y., Zhao, C.Y., 2012. A phase field model for heat transfer in a metal foam-embedded latent thermal energy storage (LTES) system. In: Proceedings of the 8th International Symposium on Heat Transfer (ISHT-8), Tsinghua University, Beijing, China.

Laboratory for Scientific Computing, University of Cambridge, 2010. http://www.lsc.phy.cam.ac.uk/research/porous_media.shtml

Provatas, N., Elder, K., 2010. Phase-Field Methods in Materials Science and Engineering. John Wiley & Sons, Germany.

Tian, Y., Zhao, C.Y., 2009. Numerical investigations of heat transfer in phase change materials using non-equilibrium model. In: Proceedings of 11th UK National Heat Transfer Conference (UKHTC-11), Queen Mary College, University of London, UK.

Tian, Y., Zhao, C.Y., 2011a. A numerical investigation of heat transfer in phase change materials (PCMs) embedded in porous metals. Energy 36, 5539–5546.

Tian, Y., Zhao, C.Y. 2011b. Natural convection investigations in Porous Phase Change Materials. Nanosci. Nanotech. Lett. 3(6), 769–772

Tian. Y., Zhao, C.Y., 2013. A Thermal and exergetic analysis of Metal Foam-enhanced Cascaded thermal Energy storage (MF-CTES). Int. J. Heat Mass Tran. 58(1–2), 86–96.

Tian, Y., Zhao, C.Y., Lapkin A., 2012. Exergy optimisation for cascaded thermal storage. In: Proceedings of the 12th International Conference on Energy Storage (Innostock 2012). University of Lleida, Lleida, Spain.

Whitaker, S., 1969, Advances in the theory of fluid motion in porous media, Ind. Eng. Chem. 12, 14-28.

Zalba, B., Marin, J.M., Cabeza, L.F., Mehling, H., 2003. Review on thermal energy storage with phase change: materials, heat transfer analysis and applications. Appl. Therm. Eng. 23, 251-283.

Zhao, C.Y., Lu, W., Tian, Y., 2010. Heat transfer enhancement for thermal energy storage using metal foams embedded within phase change materials (PCMs). Sol. Energy 84, 1402–1412.

Zhou, D., Zhao, C.Y., 2011. Experimental Investigations on Heat Transfer in Phase Change Materials (PCMs) Embedded with Porous Materials. Appl. Therm. Eng. 31, 970–977.

Zukauskas, A.A., 1987. Convective heat transfer in cross-flow, handbook of single-phase heat transfer. Wiley, New York.